Sequentially PVD-Grown Indium and Gallium Selenides Under Compositional and Layer Thickness Variation: Preparation, Structural and Optical Characterization

Martina Schmid,* Mithuran Ketharan, Jan Lucaßen, and Ihab Kardosh

Group IIIA metal chalcogenides are an auspicious material system due to their variability of properties and hence the multitude of application options, for example, in the fields of optoelectronic, thermoelectric, piezo-, and ferroelectric devices. Indium and gallium selenide films are innovatively grown in a sequential PVD (physical vapor deposition) process starting from metal precursor layers of various thicknesses, which are then subject to chalcogenization in different selenium contents. The resulting thin films are investigated for structural and optical properties by Raman, XRD (X-ray diffraction), and UV–Vis–NIR spectrometry, revealing that all the compounds In_2Se_3, InSe, In_4Se_3, Ga_2Se_3, and GaSe as well as different polytypes can be achieved depending on the metal/chalcogen ratio. Results from Raman and XRD spectroscopy are highly consistent, and also from the optical measurements changes in absorption characteristics can be correlated. The results indicate, that by fine-tuning the selenium content, deliberately growing ultra-thin layers of the different indium and gallium phases will be possible, thus opening up a promising route for 2D material fabrication. Given the scalability of the fabrication method, it is highly promising for large-scale deployment of the materials.

1. Introduction

Group IIIA metal chalcogenides are a highly promising material system due to the variability of properties not just as a function of composition but also of layer thickness. They are compound semiconductors consisting of group IIIA metals (In or Ga) and chalcogen elements (S, Se, or Te, amongst which we will focus on Se). Their layered structure is characterized by strong in-plane interactions paired with weak van der Waals bonds perpendicularly. Bulk InSe and GaSe have been utilized for frequency conversion, that is, second harmonic generation, and generation and detection of broadband tunable terahertz (THz) radiation, respectively.[1,2]

In the context of 2D materials, InSe and GaSe have gained growing interest as an alternative to classical materials like graphene or the transition metal dichalcogenides $MoS(e)_2$ and $WS(e)_2$. While graphene is surely the most researched 2D material and is characterized by its outstanding carrier mobility, it shows a fundamental lack of bandgap. Transition metal dichalcogenides (TMDCs) reveal similar 2D behavior as graphene but very distinct semiconducting properties arising from the tunability of their bandgaps.[3] This makes them suitable for application in optoelectronic devices like transistors, photodetectors, LEDs, etc.[4] Whereas $MoS(e)_2$ and $WS(e)_2$ are commonly in focus, group IIIA metal chalcogenide 2D materials (G3AMC2DMs) are significantly less researched despite being equally promising in terms of tuneability of properties, expected direct bandgap, and high carrier mobility.[5] The classical fields of application include electronics and optoelectronics, partially in the form of heterojunction devices with other 2D materials.[6] G3AMC2DMs may additionally feature thermoelectric, piezoelectric, or ferroelectric properties enabling the integration into corresponding devices.[7–9] Their tunable and diverse properties make them also suitable for various energy-related applications like thermoelectrics, photovoltaics, or photocatalysis whilst bringing high material efficiency due to their low thickness.

The properties of G3AMC2DMs strongly depend on their layer thickness, and equally on composition and finally polytype. To access the various material properties, it is thus of ultimate importance to deliberately fabricate the different compounds and phases. In this publication, we focus on indium and gallium selenides and thus refer to the corresponding phase diagrams given by Okamoto.[10,11] The two most prominent compounds are InSe/GaSe and In_2Se_3/Ga_2Se_3, which are exactly reached for an atomic percent value of 50 and 60 selenium, respectively. Whilst not apparent in the phase diagram of Ga-Se, for In-Se several

M. Schmid, M. Ketharan, J. Lucaßen, I. Kardosh
University of Duisburg-Essen
Faculty of Physics and CENIDE
Forsthausweg 2, 47057 Duisburg, Germany
E-mail: martina.schmid@uni-due.de

The ORCID identification number(s) for the author(s) of this article can be found under https://doi.org/10.1002/admi.202301086

other compounds may occur, namely In_4Se_3, In_6Se_7, In_9Se_{11}, and In_5Se_7.

The crystal structure of InSe/GaSe builds up on quadruple layers consisting of two planes of metal atoms between two planes of chalcogenide atoms connected via strong covalent bonds. The interaction between neighboring quadruple layers is weak and their stacking decides the polytype: The 2-hexagonal ε- and β-phase show AB stacking, the 3-rhombohedral γ-phase ABC, and the 4-hexagonal δ-phase ABCD sequence, whereby the quadruple layers A, B, C, and D differ in rotational orientations and lateral offsets with respect to one another. For a detailed outline and representation of the polytypes see.[12–15] Aside from the theoretical possibilities of these phases, the most common ones found across literature are β-, γ-, and ε-InSe and ε-GaSe. Regarding In_2Se_3 and Ga_2Se_3, strongly bound Se-In-Se-In-Se quintuple layers form the basis. The subsequent stacking possibilities of the quintuple layers are non-trivial due to the complicated polymorphism and existing vacant sites. The interested reader is thus referred to [9,16,17] for insight into the detailed arrangements and space groups leading to α-, β-, and δ-polytypes. It has to be noted that literature on In-Se is significantly more abundant than for Ga-Se, but similarity is often times assumed between the two material systems. Commonly found phases in literature are α, β-, γ-In_2Se_3, and β-Ga_2Se_3. An extensive review of In-Se phases can be found in. ref. [18].

The most established bottom-up growth methods for G3AMC2DMs are CVD (chemical vapor deposition), PLD (pulsed layer deposition), and PVD (physical vapor deposition), whereby for the latter mostly powders are heated in a quartz tube and the vaporized material is deposited onto the inserted substrate.[6] Only rarely co- or alternate evaporation of the elements is reported.[19] In the present paper, we innovatively fabricate binary In-Se and Ga-Se with various thicknesses and compositions in a sequential PVD process by deposition of thin In or Ga films and subsequent selenization at high temperatures. Importantly, in contrast to the literature,[20] selenium is only added during the rapid thermal processing step and is not part of the precursor stack. Fabrication details can be found in the experimental section, the naming of the samples results from the metal precursor layer thickness and the selenization condition. We investigate the compound and phase evolvement by Raman spectroscopy and X-ray diffraction (XRD). To address the optical properties, we perform UV–Vis–NIR photospectrometry and determine the absorption behavior. Finally, we also look into the stability of the thin films since degradation of In-Se and Ga-Se has been thematized in literature before.[12,21]
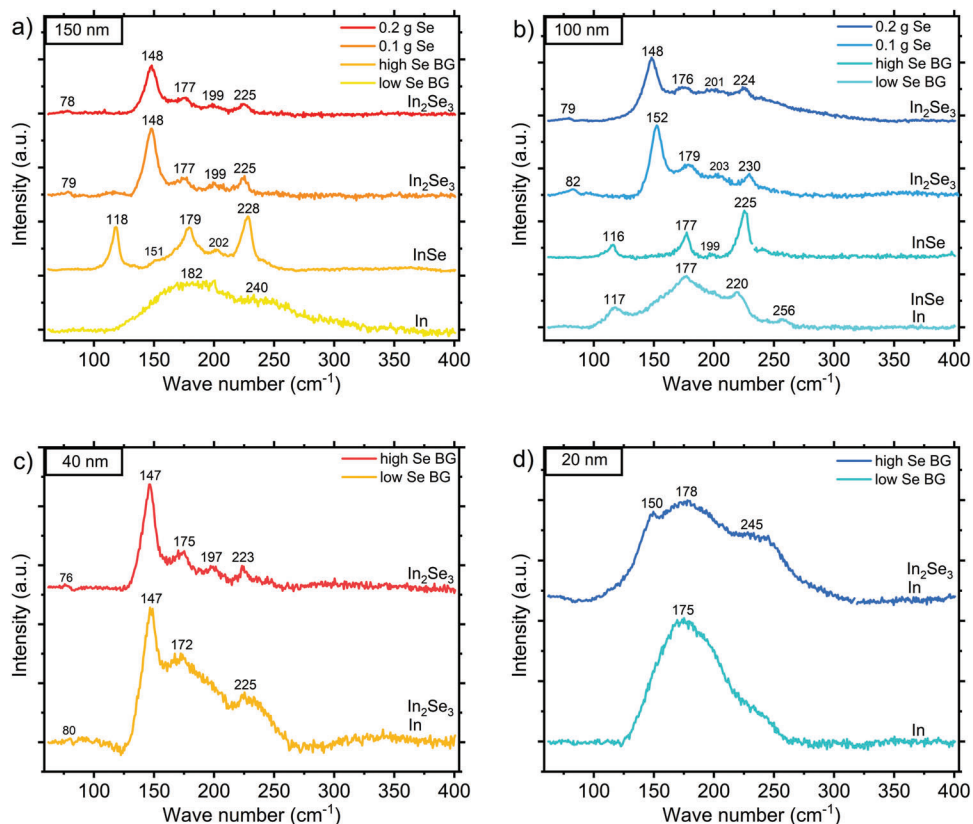
2. Results and Discussion

2.1. Raman Spectroscopy

Comparative Raman spectra for the samples of a given initial In/Ga thickness and subject to selenization under various Se content are shown in **Figures 1** and **2** for In-Se and Ga-Se, respectively. Starting from 150 nm In precursor (Figure 1a), we observe for high selenium content Raman peaks at ≈78, 148, 177, 199, and 225 cm⁻¹ with slight variations for the two cases of 0.2 and 0.1 g Se. These peaks identify In_2Se_3 and the assumed polytype is the γ-phase. Liu et al. reported the following polytype-specific

Raman resonances: 88, 104, 159, 179, 193, and 250 cm⁻¹ for α-In_2Se_3, 109, 176, and 205 cm⁻¹ for β-In_2Se_3, and 81, 95, 150, 177, 203, and 228 cm⁻¹ for γ-In_2Se_3.[22] Given the absence of Raman peaks at 104–109 and at 250 cm⁻¹ in our spectra, we rule out α- and β-phases and conclude the presence of γ-In_2Se_3 in our samples. This result also fits well with the phase diagram, where γ-In_2Se_3 is reported for temperatures above 200 °C. Small systematic variations from literature peak values may be explained by differences in fabrication method, processing temperature, substrate used, layer thickness, or measuring wavelength as also stated in the above reference (slight red-shift of the Raman peaks for 532 nm laser).[22] As the Se content is reduced, a pronounced change of Raman spectra is observed leading to peaks at 118, 179, 202, and 228 cm⁻¹ in the case of high Se background. Clearly, a phase change occurred and the resulting phase is InSe. For all three reported polytypes β-, γ-, and ε-InSe the reported Raman peak positions are similar and can be found at 116, 176, 201 (not for β), and 228 cm⁻¹.[14,23] As the peak at 201 cm⁻¹ is excluded for β-InSe but appears in our measurements, we exclude this polytype and are left with the two options of γ-, and ε-InSe. In addition, a feature at 151 cm⁻¹ occurs for 150 nm In precursor selenized in high Se BG, which can be attributed to the compound In_4Se_3.[24] For the lowest selenium content finally, only a broad peak remains with a maximum of ≈182 cm⁻¹ and a shoulder at 240 cm⁻¹. This signal is characteristic of elemental indium, see our Raman measurement on a 40 nm In film depicted in Figure S1 (Supporting Information).

Moving on to the 100 nm In precursor films (Figure 1b), we can observe a very similar behavior as for the slightly higher initial indium thickness. The Raman peaks for the samples annealed at 0.2 and 0.1 g Se are again related to γ-In_2Se_3 with a slight shift toward larger wavenumbers for the latter case. It appears that the sample 100 nm In, 0.1 g Se is an outlier as it is the only In_2Se_3 sample showing distinct shifts in the wavenumbers. For all the other In_2Se_3 samples, despite variations in In and Se supply, a minor shift of Raman peak positions occurs with a maximum of 2 cm⁻¹ toward lower wavenumbers for 40 nm In, low Se BG. The latter is in agreement with the shifts observed for Ga_2Se_3 with decreasing Se content, see below. Apparently, for 100 nm In, 0.1 g Se the phase starts to become distorted, and a transition to InSe is found for the high and in this case also for the low Se background. Whereas both samples of 100 nm In precursor and Se BG show the characteristic peaks of InSe, the lower selenium content case reveals an underlying broad feature with a strong similarity to the pure indium peak. Thus, the InSe phase is still dominating here, but the presence of In is already given. Overall, it is noted, that small shifts of the peak positions in the order of a few inverse centimeters occur. This observation may be attributed to the polycrystalline growth expected for our films and a different degree of compactness, which also can be related to the occurrence of defects.

As the indium precursor thickness is reduced, that is, 40 or 20 nm In (see Figure 1c,d), the Raman features characteristic for γ-In_2Se_3 reappear. They are clearly visible for 40 nm In, high Se BG, and become superimposed by the indium signal for 40 nm, low Se BG, and more pronouncedly for 20 nm, high Se BG. Additionally, the signal broadens ≈250 cm⁻¹, which may be an indication of the simultaneous appearance of α-In_2Se_3. In the case of 20 nm, low Se BG only the broad peak of pure

2301086 (2 of 12)

**ADVANCED
SCIENCE NEWS**

www.advancedsciencenews.com

**ADVANCED
MATERIALS
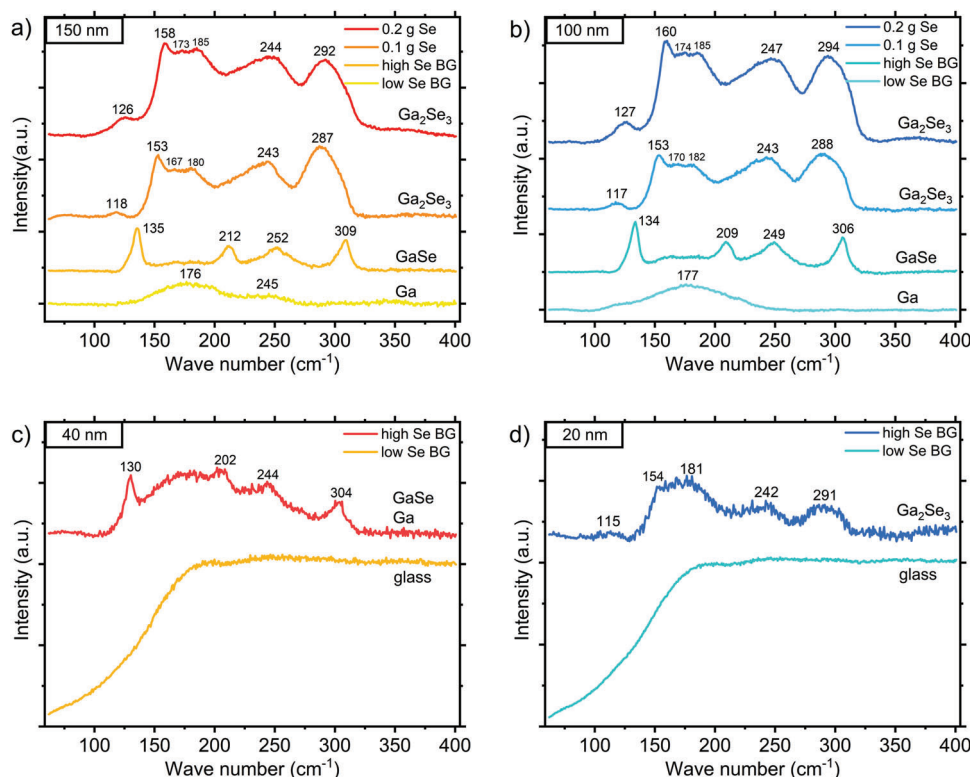INTERFACES**
Open Access

www.advmatinterfaces.de

Figure 1. Raman spectra of In-Se fabricated in a sequential process from evaporated In precursor layers of a) 150 nm, b) 100 nm, c) 40 nm, and d) 20 nm and selenized in various Se content (BG = background).

indium remains. The most striking result is the direct transition from γ-In_2Se_3 to In without any observation of InSe. Whereas for the thicker precursor films, a stochiometric phase could be achieved for low selenium contents, the thinner indium precursor films do not allow the required fine-tuning but directly transit from the selenium-rich phase to the absence of selenium integration. Consequently, for the fabrication of extremely thin InSe layers, highly precise control over selenium pressure appears crucial.

In Figure 2, the Raman spectra for the Ga-Se films are shown. Similar to In-Se, the thick precursor films (150 and 100 nm, Figure 2a,b) selenized under high Se content (0.2 and 0.1 g) exhibit Raman peaks characteristic of the selenium-rich Ga_2Se_3 compound. In our measurements, they are located at on average 126, 159, 174, 185, 245, and 293 cm^{-1} for 0.2 g Se, whereas slightly smaller numbers of on average 118, 153, 168, 181, 243, and 287 cm^{-1} are found for 0.1 g Se. Literature specifies 119, 156, 190, 240, and 289 cm^{-1} for α-Ga_2Se_3,[25] and 119, 155, 184 (bulk), 230 (bulk), 252, and 296 cm^{-1} for β-Ga_2Se_3.[26] The literature values for the two polytypes are highly similar with variations between 180 and 250 nm also depending on bulk or 2D properties. A consistent shift to higher or lower wavenumbers is however not given. Thus, first, no clear attribution to α- or β-phase is possible from our Raman spectra but both polytypes could equally be present. Second, the shift to smaller wave numbers with decreasing selenium content needs to have a different reason which may be found in the number of defects and a gradual transi-

tion to a less Se-rich phase. Third, our experiments reveal a clear peak at 126 cm^{-1} for the Se-richest samples, replacing the one at 118 cm^{-1}. This would rather be typical for GaSe when looking into Raman databases,[27] and close to the one at 133 cm^{-1} reported for GaSe below. Pure Se would however be expected to show peaks at 255 cm^{-1} or 238 and 141 cm^{-1} for the amorphous or crystalline case, respectively.[28] The shifts toward higher wavenumbers for higher Se content and toward lower ones for higher Ga ratio are consistent trends visible within the samples of 150 and 100 nm Ga and 0.2 and 0.1 g Se. Lattice distortions may be the reason for trends toward larger lattice parameters for the higher content of larger atomic radius selenium.

For the thick Ga precursors selenized in selenium background only, the GaSe phase is identified for both 150 and 100 nm Ga, high Se BG. The peaks are located at 135, 212, 252, and 309 cm^{-1} for the first and shifted to on average 3 cm^{-1} lower wave numbers for the latter. The values can be brought in line with literature data of 134, 213, 249, and 307 cm^{-1} for β-GaSe,[29] or 133, 212, 250, and 307 cm^{-1} for γ- and ε-GaSe.[30,31] No specific peaks were ruled out in these references for one or the other polytype, so Raman measurements will not allow a differentiation. For the lowest selenium content of low Se BG, any characteristic features of Ga-Se compounds are absent from the Raman spectra of 150 and 100 nm Ga precursor. Only a broad peak $\approx$176 cm^{-1} with a shoulder toward 245 cm^{-1} is left, which can be correlated to pure gallium (see the measurement on a 40 nm Ga film depicted in Figure S1, Supporting Information). In this case, the selenium

**ADVANCED
SCIENCE NEWS**

www.advancedsciencenews.com

**ADVANCED
MATERIALS
INTERFACES**

www.advmatinterfaces.de

Figure 2. Raman spectra of Ga-Se fabricated in a sequential process from evaporated Ga precursor layers of a) 150 nm, b) 100 nm, c) 40 nm, and d) 20 nm and selenized in various Se content (BG = background).

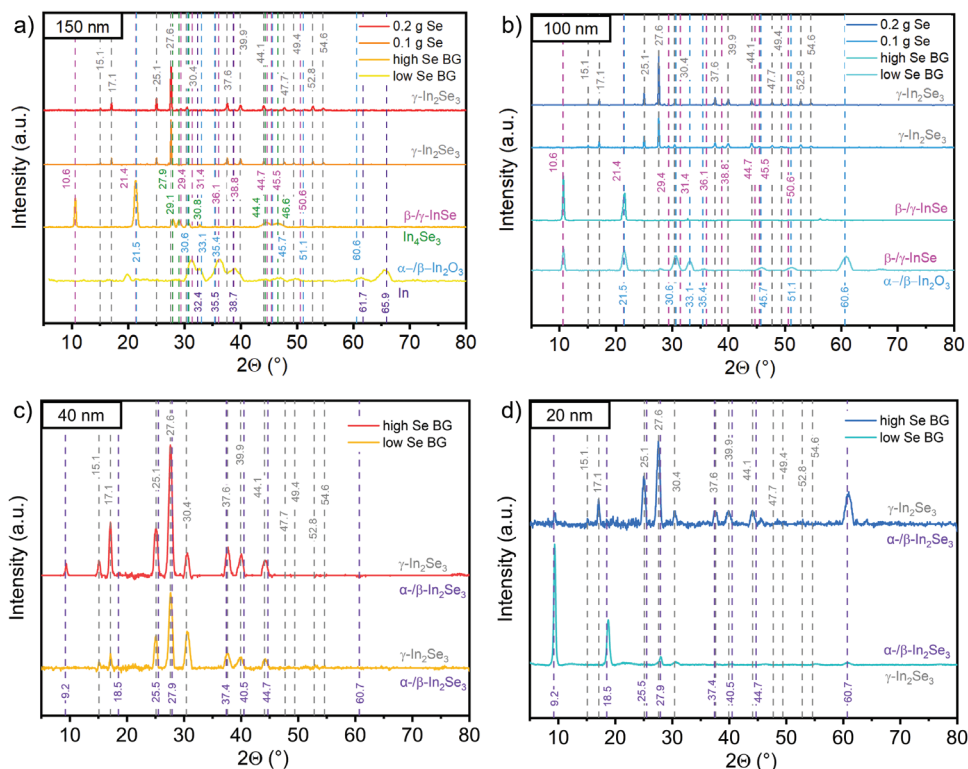content is too low to form a detectable gallium selenide compound.

As the gallium precursor thickness is reduced to 40 or 20 nm (Figure 2c,d), high Se BG leads to the formation of Ga-Se compounds, which are related to GaSe for the first and to Ga_2Se_3 for the latter case. The peak positions are similar to the ones described for the thicker precursor films with a trend to lower wave numbers. This is in line with the above observations of decreasing selenium content. Most importantly, a GaSe-phase is achieved for the ultrathin films, which was not given for InSe. This observation underlines, that a fine-tuning of the Se-content will be the key to obtaining stoichiometric phases for ultrathin and ultimately 2D films. In addition to the Ga-Se compounds, the Raman spectra for these thin films also reveal the presence of Ga which can be seen by the broad background peak that occurs most pronouncedly for 40 nm Ga, high Se BG.

When moving to the condition of low Se BG annealing, the Raman signal of both 40 and 20 nm Ga precursor films only reveals the characteristic of glass (compare the reference measurement shown in Figure S1, Supporting Information). Any characteristic feature of Ga-Se disappeared so that no detectable film is present in these samples. Compared to indium, where we still found a Raman signal for these thin films, the gallium-containing films are thinner (Ga being the smaller atom), so the material volume is smaller. It shall be noted that Raman spectroscopy is a volume-sensitive measurement and the signal reveals the dominant material in the measurement cone. To become surface-sensitive and detect extremely thin films, we next move on to XRD analysis.

3. X-Ray Diffractometry

The XRD spectra were taken under grazing incidence configuration, that is, they are sensitive to the surface compounds. Therefore, we expect to find differences compared to bulk-sensitive methods like Raman spectroscopy, when the material is inhomogeneous and the surface layer differs from the material with the largest volume share. **Figures 3** and **4** show the XRD spectra for the various In-Se and Ga-Se samples, respectively. In addition to the measurement data, lines are shown, which correspond to the peak positions of XRD results from databases for related different compounds and polytypes. The indicated angles originate from these literature values and can be correlated with our measurement data for a conclusion about existing phases. The prominent phases are mentioned with each spectrum in the sequence of decreasing amounts of occurrence as judged from spectra fitting. The respective database files are indicated in Table S1 (Supporting Information) for In-Se and Table S2 (Supporting Information) for Ga-Se, and are taken from the Crystallography Open Database,[32] the FIZ Karlsruhe – Leibniz Institute for Information Infrastructure (ICSD)[33] or Springer Materials (SD for In_4Se_3).[34]

Starting with In-Se, the 150 nm In precursor (Figure 3a) selenized in a high content of selenium (0.2 or 0.1 g Se) shows prominent peaks around the lines at 17.1°, 25.1°, 27.6°, 37,6°, 39.9°, and 44.1°, followed by some smaller ones. They are characteristic for γ-In_2Se_3 and can equally be found for 100 nm In precursor selenized in high selenium content (0.2 or 0.1 g Se,

2301086 (4 of 12)

ADVANCED
SCIENCE NEWS

www.advancedsciencenews.com

ADVANCED
MATERIALS
INTERFACES
Open Access

www.advmatinterfaces.de

Figure 3. XRD spectra of In-Se fabricated in a sequential process from evaporated In precursor layers of a) 150 nm, b) 100 nm, c) 40 nm, and d) 20 nm and selenized in various Se content (BG = background).
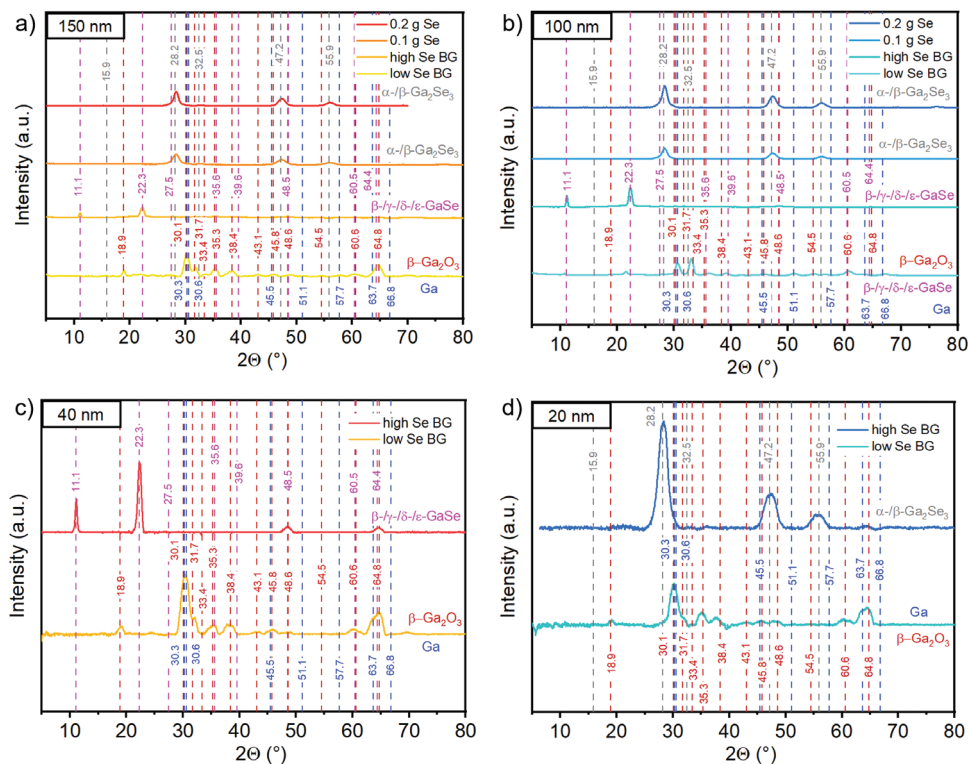
Figure 4. XRD spectra of Ga-Se fabricated in a sequential process from evaporated Ga precursor layers of a) 150 nm, b) 100 nm, c) 40 nm, and d) 20 nm and selenized in various Se content (BG = background).

**ADVANCED
SCIENCE NEWS**

www.advancedsciencenews.com

**ADVANCED
MATERIALS
INTERFACES**
Open Access

www.advmatinterfaces.de

Figure 3b). Thus, we can confirm the selenium-rich phase In_2Se_3 as well as the γ-polytype derived from Raman measurements. Still, for the thick In precursor films (150 and 100 nm In) but annealed in high Se background only, the prominent peak positions change toward the lines at 10.6° and 21.4°. These diffraction angles correspond to β- or γ-InSe and are discussed in the literature to depict the (0,0,2) and (0,0,4) orientation of β-InSe or the (0,0,3) and (0,0,6) orientation for γ-InSe.[14] According to that reference, β- and ε-InSe are highly similar in spectra, so also the latter phase cannot be excluded here. However as we exclude the β-phase from Raman measurements, we similarly need to exclude the ε-phase and conclude the existence of γ-InSe. Higher orders with diffraction angles of InSe at ≈29/31° and 45/46° are barely visible and can become rather dominated by other phases.

Namely, for 150 nm In precursor selenized in high Se background, multiple further peaks occur close to the lines at 27.9°, 29.1°, 30.8°, 44.4° and 46.6°. They can be linked to In_4Se_3, which according to the phase diagram is expected in a small range below stoichiometry only. A proof of this phase, even if it just seems to appear at the surface (and not in Raman spectroscopy) is promising for the accessibility of this compound in our fabrication approach. Some remainders of In_4Se_3 peaks might still be identified for 150 nm In precursor and low selenium background. Yet, they become dominated by the occurrence of α-/β-In_2O_3 – as indicated by peaks approaching the lines at 21.5°, 30.6°, 33.1°, 35.4°, 45.7°, 51.1, and 60.6° – and of pure In related to the lines at 32.4°, 35.5°, 38.7°, 61.7°, and 65.9°. For 100 nm In precursor selenized in high Se background, only the two first peaks of InSe stick out. In the case of annealing in low Se background, the second peak of InSe could also be attributed to In_2O_3 again as there is a good match of the higher-order peaks with the other In_2O_3 lines. Thus, we can conclude that for the minimum addition of selenium, the lack of this element is quickly compensated by oxygen. However, when sufficient selenium is present, the In-rich In_4Se_3, the stoichiometric InSe, or the Se-rich In_2Se_3 compound can be formed.

For the thinner In precursors (40 and 20 nm shown in Figure 3c,d, respectively), despite selenization in selenium background only, the observed phases are again selenium-rich so that only In_2Se_3 characteristic peaks occur. For high Se BG, the characteristic γ-In_2Se_3 peaks at 15.1°, 17.1°, 25.1°, 27.6°, 30.4°, 37.6°, 39.9°, and 44.1° are all present. Additionally, signs of α-In_2Se_3 occur with peak lines at 9.2°, 18.5°, 25.5°, 27.9°, 37.4°, 40.5°, 44.7°, and 60.7°. They appear more or less pronounced compared to the peaks of γ-In_2Se_3 and become dominant for low selenium background and 20 nm In precursor. The preferential occurrence of the low-temperature α-phase may be linked to the lower pressure when annealing in a selenium background atmosphere only. In particular, for the case of low Se BG, the graphite boat containing the samples was left open so that the overall heat distribution may be different. On the other hand, corresponding to the databases, the characteristic peaks of α- and β-In_2Se_3 are highly similar, so that also the β-phase could be the one present and it would fit well with the processing temperatures. Aside from that, peaks for In_2O_3 are not found here, underlining that a sufficient In/Se ratio can prevent oxidation.

From the XRD analysis of Ga-Se (see Figure 4), we find a generally similar behavior as for In-Se and parallels to results from Raman analysis. The thick Ga precursor films (150 and 100 nm, Figure 4a,b) anneal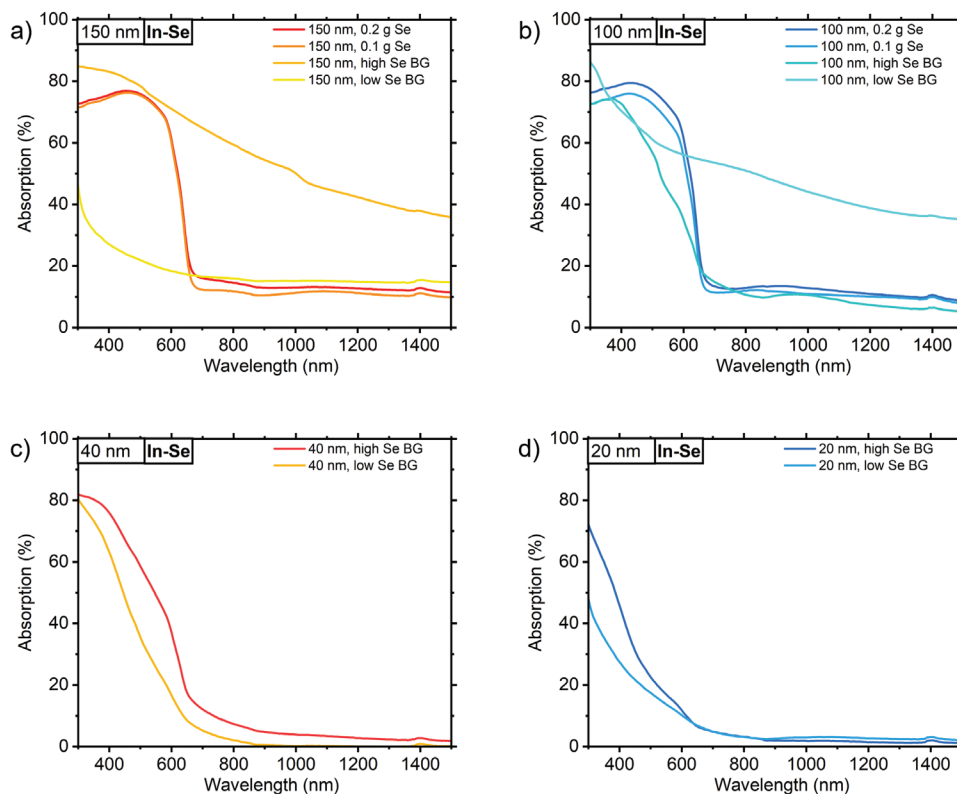ed in high selenium content (0.2 or 0.1 g Se) reveal three main characteristic peaks at the lines of 28.2°, 47.2°, and 55.9°, which are representative for α- and β-Ga_2Se_3. The same result was found from Raman spectroscopy. With reducing selenium content, these peaks disappear, and for high selenium background new peaks appear at the lines of 11.1° and 22.3°. These angles are typical for all polymorphs of GaSe (β-/γ-/δ-/ε-), which thus cannot be distinguished in our XRD analysis as it was the case in Raman spectroscopy of GaSe. What is interesting to see is that whilst Raman spectroscopy only shows indications for elemental Ga in the case of low Se background, XRD analysis reveals additional characteristic peaks for β-Ga_2O_3. The most prominent lines of the latter can be correlated with peaks around the values of 18.9°, 30.1°, 33.4°, 35.3°, 38.4° 45.8°, 48.6°, 60.6°, and 64.8°, generally prevailing over the ones for Ga, which are a ≈30.5°, 45.5°, and 64°/67°. The bulk-sensitive method Raman spectroscopy did not indicate the existence of Ga_2O_3, so we assume it is only present as a thin surface layer accessible in XRD.

For In-Se we were not able to identify the stoichiometric compound of InSe for the thinner films. In the case of Ga-Se, however, the 40 nm Ga precursor film selenized in a high selenium background (see Figure 4c) reveals the characteristic lines for β-/γ-/δ-/ε-GaSe, even including one at the higher angle of 48.5°. For the 20 nm Ga precursor film selenized under the same conditions, however, α-/β-Ga_2Se_3 is identified (compare Figure 4d). The XRD spectra for the thinner films (40 and 20 nm Ga) selenized in a low Se background can clearly be attributed to β-Ga_2O_3 and Ga with a stronger prominence of the oxide for the 40 nm precursor film and of the pure metal for the 20 nm Ga precursor (according to XRD fitting procedures). The pronounced occurrence of the oxidic phase makes us understand why Raman spectroscopy revealed characteristics resembling the one of pure glass only. At the same time, it confirms that oxidation is more severe for Ga compared to In compounds as it was also stated in the literature.[12] The important point to find out will be if oxidation can be restricted to a very thin surface layer and if this may be negligible compared to the remaining GaSe film underneath. We could not observe the coexistence of Ga_2O_3 with Ga_2Se_3, which may be because if sufficient selenium is supplied, the risk of oxidation is lower.

In this context, Figure S2 (Supporting Information) shows Raman spectra of GaSe, prepared by selenization in high Se background of a 40 nm Ga precursor film after different times of exposure to air: immediately after preparation, after having passed the various characterization measurements (rep) and finally after staying outside the desiccator for three days (Ox). With increasing exposure time, the overall intensity of the Raman signal decreases, as also known from the literature,[21] but the main peaks remain visible. They only appear slightly shifted toward larger wavenumbers for ≈5 cm^{-1}, yet no attribution to a different phase is given. This observation can be seen as an indication that despite Ga-Se is prone to oxidation when lacking selenium, bulk GaSe persists.

4. Optical spectroscopy

Transmission and reflection show a very particular behavior that can be correlated to the phase changes observed with varying selenium content. The condensed view on absorption, emerging as the remaining summand to add up transmission and reflection

**ADVANCED
SCIENCE NEWS**

www.advancedsciencenews.com

**ADVANCED
MATERIALS
INTERFACES**
Open Access

www.advmatinterfaces.de

Figure 5. Absorption spectra of In-Se fabricated in a sequential process from evaporated In precursor layers of a) 150 nm, b) 100 nm, c) 40 nm, and d) 20 nm and selenized in various Se content (BG = background).
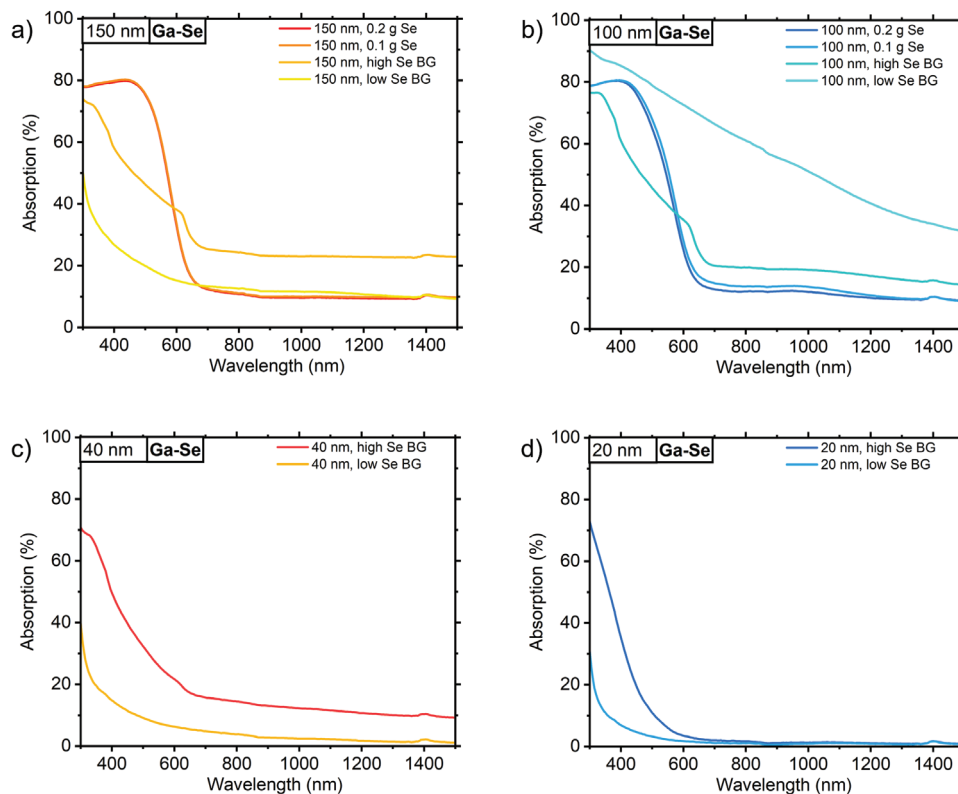
to one, is represented in **Figure 5** and **6** for In and Ga compounds, respectively. From the absorption characteristics, the wavelength at the maximum slope is extracted and converted to energy. We label this value as E @ max $(dA/d\lambda)$ or short E_{drop} and give the numbers in **Tables 1** and **2**.

As we can observe from Figure 5 for In-Se, the absorption characteristic for 150 and 100 nm. In both with 0.2 and 0.1 g Se is highly comparable with a maximum close to 80% up to a wavelength of ≈600 nm and a sharp drop to less than 20% thereafter. The extracted value for E_{drop} is identically 1.94 eV. Following Raman and XRD analysis, these samples consist of γ-In_2Se_3. A similar optical behavior is found for the samples with 100 and 40 nm In selenized in high Se BG. Just the drop is less steep and the value E_{drop} amounts to slightly higher values of 1.96 and 1.97 eV, respectively. According to XRD measurements, the In_2Se_3 phase is only present for the here-discussed thinner film, whereas InSe dominates for the thicker one. 40 nm In, low Se BG, which is expected to be In_2Se_3 as well, shows the same maximum absorption of 80% followed by a pronounced drop. Yet, the drop is shifted toward shorter wavelengths corresponding to 2.95 eV and the increase may be related to the transition from γ- to α-phase or to the starting coexistence of indium. For the samples with 20 nm In precursor, the drop flattens further and the maximum absorption in the investigated wavelength range down to 300 nm reduces since E_{drop} is shifted to higher energies of 3.10 and 4.13 eV for high and low Se BG, respectively. Indications for In_2Se_3 are still found in the XRD spectra, whereas Raman measurements point to the increasing dominance of In. Similarly high values

for E_{drop} are also observed for 150 nm In, low Se BG (4.13 eV), and for 100 nm In, low Se BG (3.80 eV), whereby the absorption is by a factor of two larger for the latter one. It may indicate, that in addition to the indium signal, the characteristics of InSe are visible. Thus, the absorption spectra for 100 nm In, low Se BG, and for 150 nm In, high Se BG have comparable high absorption with a very shallow drop, just the value E_{drop} is with 2.41 eV smaller for the latter case due to the lower indium content.

In Table 1, the values for E_{drop} are also juxtaposed to the In/Se ratios resulting from X-ray fluorescence (XRF) measurements. A clear correlation of low E_{drop} to small In/Se ratios and of large numbers for In-rich cases can be found. The table further correlates the phases derived from Raman and XRD measurements, linking low E_{drop} values to In_2Se_3, increasing ones to InSe, and the highest numbers finally approaching 4.13 eV to the predominance of In. Again, it becomes visible that XRD as a surface-sensitive method can still reveal In_2Se_3 phases whilst XRF, Raman, and optical measurements disclose the predominance of indium.

The optical behavior for Ga-Se (Figure 6) is highly comparable to the one of In-Se. The main difference is a shift to shorter wavelengths for the absorption drop and hence overall higher values for E_{drop}. In detail, a high absorption of ≈80% followed by a clear drop corresponding to 2.12–2.19 eV terminates in a low absorption below 20% for the Ga_2Se_3 samples (150 and 100 nm Ga, 0.2 and 0.1 g Se). The samples related directly to GaSe by Raman spectroscopy (150, 100 nm, and 40 nm Ga, high Se BG) reveal a similar very distinct shape characterized by an

**ADVANCED
SCIENCE NEWS**

www.advancedsciencenews.com

**ADVANCED
MATERIALS
INTERFACES**
Open Access

www.advmatinterfaces.de

Figure 6. Absorption spectra of Ga-Se fabricated in a sequential process from evaporated Ga precursor layers of a) 150 nm, b) 100 nm, c) 40 nm, and d) 20 nm and selenized in various Se content (BG = background).

absorption above 70% for short wavelengths, an initial steep drop which can be correlated to an energy of $\approx$3.22–3.26 eV that then flattens until a kink with another steep drop $\approx$2.0 eV occurs and leads to a saturation of the absorption $\approx$20%. According to XRD spectroscopy, also the sample 100 nm Ga, low Se BG should contain GaSe (asides from Ga), and here we observe the same as for two InSe samples in Figure 5a,b), namely an overall high absorption with a slight drop only. The related E_{drop} equals 4.13 eV just as for samples with dominating gallium (150, 40, 20 nm Ga, low Se BG) and indium. The reason is simply that this value corresponding to 300 nm is the lower limit of our range of investigation and thus indicates that the true E_{drop} is $\geq$ 4.13 eV. The values of E_{drop} for Ga-Se are given in Table 2 and can again be well correlated to the results from XRF measurements providing Ga/Se ratios below 0.5 for the Ga_2Se_3 samples with $E_{drop} \approx$2 eV, ratios $\approx$1 for GaSe with E_{drop} of $\approx$3 eV, and significantly larger values when Ga dominates which is linked to an absorption drop at the edge of our characterization range.

Across the literature, bandgap values for In-Se and Ga-Se compounds are found that have a trend toward lower values compared to E_{drop} which we derived from the point of highest slope in the absorption characteristic. Thus, to complement our approach of E_{drop} extraction initially chosen for unbiased information about the absorption characteristics, we address a potential derivation of bandgaps from Tauc plots and calculate the absorption coefficient following Equation (1) given in the Experimental part. The thickness required for this step is obtained from profilometry, transmission and reflection are the ones measured by opti-

cal spectroscopy. The absorption coefficient is then plotted in the form of either $(\alpha E)^2$ or $(\alpha E)^{1/2}$ versus the energy E to find a linear fit delivering the value of either the direct or indirect bandgap. Figures S3 and S4 (Supporting Information) represent the $(\alpha E)^2$ and $(\alpha E)^{1/2}$ plotting for the In-Se samples and Figures S5 and S6 (Supporting Information) correspondingly for Ga-Se. For both plotting options, areas suitable for linear fitting can be identified. Generally, the choice of fit ranges is clearer for the samples with higher selenium content, whereas for lower selenium content, the investigated energy range becomes the limiting factor.

The resulting bandgap values are summarized in Tables 1 and 2 and are discussed in the following. Literature generally reports direct bandgaps for G3AMC2DMs, therefore we start with the corresponding analysis. For In-Se, our direct bandgap fitting delivers consistently 1.9 eV for γ-In_2Se_3, and slightly lower values $\approx$1.6 eV for α-In_2Se_3. High bandgap values for the cases of dominating In, just as expected from the E_{drop} values, are not observed in direct bandgap fitting but the values stay at 1.5–1.6 eV. Looking at the alpha plots for these samples (see Figure S3, Supporting Information), it is to be noted that due to the limited measurement range, the corresponding fits are valid with restrictions. Bandgap values of 1.6–1.9 eV for In_2Se_3, however, align very well with the numbers reported in the literature.[35,36] For InSe, a bandgap range from 1.25 eV (bulk) to 2 eV (2 layers) was published.[37] Assuming that our samples are thin, this might be brought in line with $E_{g,dir} =$ 1.8 eV derived for the sample 100 nm In, high Se BG, which is attributed to InSe by Raman and XRD characterization. Most interestingly, for the other two samples

Table 1. Comparative overview on characterization results obtained from In-Se samples fabricated in a PVD-based sequential growth: compositional ratios from XRF, phases from Raman and XRD, energy E_{drop} at steepest slope of absorption from optical spectroscopy, and bandgap energy derived from fitting direct or indirect band transitions ($E_{g,dir}$ and $E_{g,indir}$).

	In/Se	Raman	XRD	E_{drop} [eV]	$E_{g,dir}$ [eV]	$E_{g,indir}$ [eV]
150 nm, 0.2 g Se	0.30	In_2Se_3	In_2Se_3	1.94	1.9	1.7
150 nm, 0.1 g Se	0.31	In_2Se_3	In_2Se_3	1.94	1.9	1.7
150 nm, high Se BG	0.69	InSe	InSe, In_4Se_3	2.41	0.8	0.6
150 nm, low Se BG	7.76	In	In, In_2O_3	4.13	1.6	2.9
100 nm, 0.2 g Se	0.31	In_2Se_3	In_2Se_3	1.94	1.9	1.7
100 nm, 0.1 g Se	0.31	In_2Se_3	In_2Se_3	1.94	1.9	1.8
100 nm, high Se BG	0.49	InSe	InSe	1.96	1.8	1.6
100 nm, low Se BG	2.57	InSe, In	InSe, In_2O_3	3.80	0.7	2.0
40 nm, high Se BG	0.42	In_2Se_3	In_2Se_3	1.97	1.6	1.6
40 nm, low Se BG	0.42	In_2Se_3, In	In_2Se_3	2.95	1.7	1.6
20 nm, high Se BG	0.45	In_2Se_3, In	In_2Se_3	3.10	1.7	1.5
20 nm, low Se BG	0.51	In	In_2Se_3	4.13	1.5	1.4

expected to also contain InSe (150 nm In, high Se BG, and 100 nm, low Se BG), we observe $E_{g,dir}$ of 0.7–0.8 eV. The literature reports $E_{g,dir}$ = 0.8 eV for In_4Se_3,[38] which would match the additional prediction from XRD for the first sample. Yet, again the fitting range is highly restricted. The results from our indirect bandgap fitting are generally similar with overall slightly lower numbers than the extracted direct bandgaps. Only for the two cases of 150 and 100 nm In, low Se BG, for which – however amongst others – the presence of elemental In is assumed, we find $E_{g,indir} \geq 2.0$ eV. As it is visible from Figure S4 (Supporting Information), the fitting area is here again at the edge of our measurement range.

In the bandgap fitting for the Ga-Se samples, very consistently high values are derived for the samples where no Se-containing compounds were predicted by Raman and XRD measurements (150, 40, 20 nm Ga, low Se BG). The corresponding values amount to 1.9 eV ≤ $E_{g,dir}$ ≤ 2.0 eV, and 2.9 eV ≤ $E_{g,indir}$ ≤ 3.3 eV, whereby the latter range results again from fitting areas

at the edge of our measurement range (see Figures S5 and S6, Supporting Information). For the rest, the results from indirect bandgap fitting are in general 0.2–0.3 eV lower but show the same trends, so we will only discuss the direct bandgap case in more detail as it is also the prominently considered one in the literature. A very clear correlation between the predicted phases and bandgap ranges can be established, namely 1.9–2.0 eV for Ga_2Se_3 and 1.2–1.6 eV for GaSe. Only the sample 100 nm Ga, low Se BG pulls out in direct bandgap fitting with a value as low as 0.8 eV, which may be correlated to an insufficient fit range despite the higher y-values considered here (see Figure S5, Supporting Information). The literature value for the bandgap of Ga_2Se_3 is 1.9 eV,[25,26] that is, highly consistent with what we find. For GaSe in contrast, 2–3.5 eV were reported,[39] which surpasses all our calculations. Yet, we do observe a high analogy to the In-Se samples which are also characterized by a smaller bandgap of InSe compared to In_2Se_3.

Overall, we find a clear correlation between different value ranges derived for E_{drop}, $E_{g,dir}$ and $E_{g,indir}$ to distinct phases identified by Raman and XRD spectroscopy. Hereby, the values for

Table 2. Comparative overview on characterization results obtained from Ga-Se samples fabricated in a PVD-based sequential growth: compositional ratios from XRF, phases from Raman and XRD, energy E_{drop} at steepest slope of absorption from optical spectroscopy, and bandgap energy derived from fitting direct or indirect band transitions ($E_{g,dir}$ and $E_{g,indir}$).

	Ga/Se	Raman	XRD	E_{drop} [eV]	$E_{g,dir}$ [eV]	$E_{g,indir}$ [eV]
150 nm, 0.2 g Se	0.23	Ga_2Se_3	Ga_2Se_3	2.12	2.0	1.8
150 nm, 0.1 g Se	0.24	Ga_2Se_3	Ga_2Se_3	2.12	2.0	1.7
150 nm, high Se BG	1.24	GaSe	GaSe	3.22/1.98	1.6	1.4
150 nm, low Se BG	21.11	Ga	Ga, Ga_2O_3	4.13	1.9	2.9
100 nm, 0.2 g Se	0.24	Ga_2Se_3	Ga_2Se_3	2.19	2.0	1.7
100 nm, 0.1 g Se	0.23	Ga_2Se_3	Ga_2Se_3	2.14	1.9	1.7
100 nm, high Se BG	0.60	GaSe	GaSe	3.22/1.97	1.6	1.4
100 nm, low Se BG	10.28	Ga	GaSe, Ga, Ga_2O_3	4.13	0.8	1.4
40 nm, high Se BG	0.73	GaSe, Ga	GaSe	3.22/2.00	1.2	1.2
40 nm, low Se BG	8.47	glass	Ga, Ga_2O_3	4.13	2.0	3.2
20 nm, high Se BG	0.36	Ga_2Se_3	Ga_2Se_3	3.26	2.0	1.8
20 nm, low Se BG	4.69	glass	Ga, Ga_2O_3	4.13	1.9	3.3

**ADVANCED
SCIENCE NEWS**

www.advancedsciencenews.com

**ADVANCED
MATERIALS
INTERFACES**
Open Access

www.advmatinterfaces.de

direct bandgap fitting are mostly in agreement with literature reports, just for the GaSe samples we predict lower bandgaps of 1.2–1.6 eV. The fitting of $(\alpha E)^2$ or $(\alpha E)^{1/2}$ is however always highly subjective and strongly dependent on the fitting range as well as on assumed layer thicknesses, which may be subject to substantial errors. Thus, we highlighted E_{drop} as a direct quantity allowing us to compare the optical properties of the different In-Se and Ga-Se samples as they would also be relevant in the applications. Importantly, we confirm that high bandgap values ≈2 eV are feasible for our In-Se and Ga-Se layers, whereby the metal-rich compounds appear more promising in this regard.

5. Conclusion

Via an original sequential process based on the thermal evaporation of an In or Ga precursor film subsequently subject to annealing in a Se atmosphere, we could successfully fabricate different phases of In-Se and Ga-Se. Tuning the precursor layer thickness as well as the amount of selenium, we achieved the stochiometric (InSe, GaSe), the Se-rich (In_2Se_3, Ga_2Se_3), and for indium the reported In-rich phase (In_4Se_3). These compunds along with possible polytypes were confirmed by Raman spectroscopy and XRD analysis. The two methods showed highly consistent results with additional phases observed by the surface-sensitive X-ray method. The identification of the different phases and transitions with changing In and Se supply was further confirmed by optical analysis where a pronounced change in absorption was found as the phase changed. Tables 1 and 2 provide a summary overview of the derived phases and band transition energies for In-Se and Ga-Se, respectively, which can also be linked to the In/Se and Ga/Se ratios as derived from XRF measurements. The results confirm that by tuning the metal/chalcogen ratio, we can grow In-Se and Ga-Se compounds of various phases and related characteristic structural and optical properties. Next to the shown optical behavior, the electrical properties of the films will need to be tested in the future.

Aside from the observation of the different phases of In-Se and Ga-Se compounds we also found indications for In_2O_3 and Ga_2O_3 from XRD analysis. The presence of these compounds on the surfaces of extremely Se-poor samples, which occurred more pronouncedly for the Ga-samples, is an indication of oxidation under lack of selenium. When a sufficient, yet fitting to the desired composition, amount of selenium was supplied, no signals of oxidic surface layers could be measured. These findings make us positive that by fine-tuning the selenium supply we will be able to fabricate the different In-Se and Ga-Se phases in a controlled way also for nano-thin films. Finally, the appearance of a surface oxidation layer, in particular Ga_2O_3, may not be a limiting factor but rather an excellent opportunity for forming pn-junction devices with this wide-gap oxidic layer that has gained growing interest, for example, in high-power applications. Given the scalability of our fabrication method, it is highly promising for large-scale deployment of the materials in various applications.

6. Experimental Section

Indium and gallium selenides were fabricated in a sequential process. First, a thin layer of indium or gallium is deposited by thermal evaporation

with thicknesses starting from 150 and 100 nm and then being reduced to 40 and 20 nm. The layer thicknesses of indium were controlled via a calibrated microbalance, those of gallium by weighing the mass of material to evaporate following prior calibration. Subsequently, the films were placed in a graphite boat within a rapid thermal processing oven for annealing in a selenium atmosphere. The amount of selenium was stepwise reduced from 0.2 g over 0.1 g of Se to a selenium background (BG) atmosphere only, which was denoted as "high" or "low" depending on whether in the process before selenium was present or outgassing at high temperatures was performed. The processing temperature of the Se-containing graphite boat followed the routing through three zones set to 20, 350, and 700 °C, respectively: starting from zone 1, 10 min in zone 2, 6 min in zone 3, 5 min in zone 2, and finishing in zone 1.

Element ratios were measured by X-ray fluorescence (Spectro XEPOS C EDXRF) and the final film thicknesses were determined by profilometry (Bruker Dektak 6 M). They were a factor of 2.5–4.5 higher than the precursor thicknesses, depending on the material.

The samples were characterized in detail by Raman spectroscopy using a custom-built Raman system by Femtika. The excitation occurs with a 532 nm cw laser focused by a 20x/0.8 objective onto the sample. After passing a multi-modal Kymera-spectrograph, the scattered light was detected by an ultrafast and ultrasensitive electron-multiplying CCD camera (both from Oxford Instrument/Andor Technology). The structural characterization was complemented by X-ray diffraction in a high-resolution Rigaku SmartLab system. The measurements were conducted in grazing incidence configuration with Cu K_α radiation.

Optical characterization was performed with a PerkinElmer Lambda 1050+ UV–Vis–NIR photo spectrometer. For measurements of total transmission T and reflection R, an integrating sphere of 150 mm diameter was employed, and the spectral range from 300 –1500 nm was chosen. The absorption A was calculated as $A = 1 - R - T$. From this value the absorption coefficient α was determined via Lambert–Beer's law knowing the layer thickness d from profilometry:

$$\alpha = \frac{1}{d} \ln \frac{1-R}{T} \tag{1}$$

Generally, the samples were stored in desiccators except for when they were subject to measurements. In certain cases, the samples were deliberately exposed to air for several days to perform oxidation tests.

Statistical Analysis: All measurements were performed on the sample centers, since toward the edges inhomogeneities and phase variations were observed.

The Raman signal was averaged over an illumination volume defined by an incident laser spot of ≈0.8 μm diameter focused on the sample surface. The step width of the measurement data was 0.6–0.7 cm^{-1}. The signal was subject to background correction and baseline subtraction. Sharp peaks originating from cosmic rays were deleted. This along with further analysis was performed in Origin. When taking repetitive measurements, variations of ≈± 1 cm^{-1} in peak position were noticed, which was extracted at the point of maximum intensity.

The X-ray diffraction measurements were performed in grazing incidence configuration (GIXRD) with a longitudinal irradiation width of ≈14 mm. The incident angle was 0.7°, or 0.2° for the thinnest samples (20 and 40 nm Ga precursor, low Se BG). Background and baseline corrections were performed on the data as well as B-spline smoothing except if any peaks disappear. The data were analyzed using the software Smartlabstudio II from Rigaku and referring to the databases cited in Tables S1 and S2 (Supporting Information).

Transmission and reflection measurements were taken with a step size of 5 nm under a light-illumination spot of ≈1 cm × 1.5 cm. For the calculation of the absorption coefficient, layer thicknesses determined by profilometry were used (except for the thinnest gallium-containing films where they are extrapolated from XRF measurements). These layer thicknesses were subject to a non-negligible error. Yet even a variation of ± 20% doesn't change the last digit of the bandgap that was given as a result of the absorption coefficient plotting (the fitting error itself in these plots was minor). Nevertheless, the analysis focused on absorption, which was

independent of thickness, and only gives the absorption coefficient and related bandgap extractions in the supplementary.

Supporting Information

Acknowledgements

Conflict of Interest

The authors declare no conflict of interest.

Data Availability Statement

The data that support the findings of this study are available from the corresponding author upon reasonable request.

Keywords

[1] J. Guo, J.-J. Xie, D.-J. Li, G.-L. Yang, F. Chen, C.-R. Wang, L.-M. Zhang, Y. M. Andreev, K. A. Kokh, G. V. Lanskii, V. A. Svetlichnyi, *Light: Sci. Appl.* **2015**, *4*, e362.

[2] K. C. Mandal, S. H. Kang, M. Choi, J. Chen, X. C. Zhang, J. M. Schleicher, C. A. Schmuttenmaer, N. C. Fernelius, *IEEE J. Sel. Top. Quantum Electron.* **2008**, *14*, 284.

[3] L. Yang, W. Chen, Q. Yu, B. Liu, *Nano Res.* **2021**, *14*, 1583.

[4] Q. H. Wang, K. Kalantar-Zadeh, A. Kis, J. N. Coleman, M. S. Strano, *Nat. Nanotechnol.* **2012**, *7*, 699.

[5] D. A. Bandurin, A. V. Tyurnina, G. L. Yu, A. Mishchenko, V. Zólyomi, S. V. Morozov, R. K. Kumar, R. V. Gorbachev, Z. R. Kudrynskyi, S. Pezzini, Z. D. Kovalyuk, U. Zeitler, K. S. Novoselov, A. Patanè, L. Eaves, I. V. Grigorieva, V. I. Fal'ko, A. K. Geim, Y. Cao, *Nat. Nanotechnol.* **2017**, *12*, 223.

[6] W. Huang, L. Gan, H. Li, Y. Ma, T. Zhai, *CrystEngComm* **2016**, *18*, 3968.

[7] H. Cai, Y. Gu, Y.-C. Lin, Y. Yu, D. B. Geohegan, K. Xiao, *Appl. Phys. Rev.* **2019**, *6*, 041312.

[8] M. Dai, C. Gao, Q. Nie, Q.-J. Wang, Y.-F. Lin, J. Chu, W. Li, *Adv. Mater. Technol.* **2022**, *7*, 2200321.

[9] C. K. Y. Tan, W. Fu, K. P. Loh, *Chem. Rev.* **2023**, *123*, 8701.

[10] H. Okamoto, *J. Phase Equilib. Diffus.* **2004**, *25*, 201.

[11] H. Okamoto, *J. Phase Equilib. Diffus.* **2009**, *30*, 658.

[12] H. Arora, A. Erbe, *InfoMat* **2021**, *3*, 662.

[13] J. Srour, M. Badawi, F. E. H. Hassan, A. Postnikov, *J. Chem. Phys.* **2018**, *149*, 054106.

[14] I. Grimaldi, T. Gerace, M. M. Pipita, I. D. Perrotta, F. Ciuchi, H. Berger, M. Papagno, M. Castriota, D. Pacilé, *Solid State Commun.* **2020**, *311*, 113855.

[15] S. Lim, J.-U. Lee, J. H. Kim, L. Liang, K. Xiangru, T. Nguyen, Z. Lee, S. Cho, H. Cheong, *Nanoscale* **2020**, *12*, 8563.

[16] W. Li, F. P. Sabino, F. Crasto de Lima, T. Wang, R. H. Miwa, A. Janotti, *Phys. Rev. B* **2018**, *98*, 165134.

[17] G. Almeida, S. Dogan, G. Bertoni, C. Giannini, R. Gaspari, S. Perissinotto, R. Krahne, S. Ghosh, L. Manna, *J. Am. Chem. Soc.* **2017**, *139*, 3005.

[18] G. Han, Z.-G. Chen, J. Drennan, J. Zou, *Small* **2014**, *10*, 2747.

[19] S. Marsillac, A. M. Combot-Marie, J. C. Bernède, A. Conan, *Thin Solid Films* **1996**, *288*, 14.

[20] R. Panda, U. P. Singh, R. Naik, N. C. Mishra, *AIP Conf. Proc.* **2019**, *2115*, 030272.

[21] O. Del Pozo-Zamudio, S. Schwarz, J. Klein, R. Schofield, E. Chekhovich, Ö. Arslan, E. Margapoti, A. Dmitriev, G. Lashkarev, D. Borisenko, N. Kolesnikov, J. Finley, A. Tartakovskii, *arXiv1506.05619v1* **2015**.

[22] L. Liu, J. Dong, J. Huang, A. Nie, K. Zhai, J. Xiang, B. Wang, F. Wen, C. Mu, Z. Zhao, Y. Gong, Y. Tian, Z. Liu, *Chem. Mater.* **2019**, *31*, 10143.

[23] S.-W. Hsiao, C.-S. Yang, H. Yang, C. H. Wu, S.-K. Wu, L. Y. Chang, Y.-T. Ho, S.-J. Chang, W. C. Chou, *Front. Mater.* **2022**, *9*, 871003.

[24] H. Bergeron, L. M. Guiney, M. E. Beck, C. Zhang, V. K. Sangwan, C. G. Torres-Castanedo, J. T. Gish, R. Rao, D. R. Austin, S. Guo, D. Lam, K. Su, P. T. Brown, N. R. Glavin, B. Maruyama, M. J. Bedzyk, V. P. Dravid, M. C. Hersam, *Appl. Phys. Rev.* **2020**, *7*, 041402.

[25] C.-H. Ho, *ACS Omega* **2020**, *5*, 18527.

[26] D. Bletskan, V. Kabatsii, M. Kranjčec, *Inorg. Mater.* **2010**, *46*, 1290.

[27] M. Bagheri, H.-P. Komsa, Computational Raman Database, ramandb.oulu.fi/ramandb/ (accessed: November 2023).

[28] A. Märkl, M. von der Emde, C. Nowak, W. Richter, D. R. T. Zahn, *Surf. Sci.* **1995**, *331–333*, 631.

[29] T. J. Wieting, J. L. Verble, *Phys. Rev. B* **1972**, *5*, 1473.

[30] M. Usman, S. Golovynskyi, D. Dong, Y. Lin, Z. Yue, M. Imran, B. Li, H. Wu, L. Wang, *J. Phys. Chem. C* **2022**, *126*, 10459.

[31] R. M. Hoff, J. C. Irwin, R. M. A. Lieth, *Can. J. Phys.* **1975**, *53*, 1606.

[32] Crystallography Open Database (COD), crystallography.net/cod/ (accessed: November 2023).

[33] Inorganic Crystal Structure Database – ICSD, icsd.fiz-karlsruhe.de (accessed: November 2023).

[34] In4Se3 Crystal Structure Database, materials.springer.com/isp/crystallographic/docs/sd_0451600, (accessed: November 2023).

[35] J. Jasinski, W. Swider, J. Washburn, Z. Liliental-Weber, A. Chaiken, K. Nauka, G. A. Gibson, C. C. Yang, *Appl. Phys. Lett.* **2002**, *81*, 4356.

[36] I. V. Bodnar, *Semiconductors* **2016**, *50*, 715.

**ADVANCED
SCIENCE NEWS**

www.advancedsciencenews.com

**ADVANCED
MATERIALS
INTERFACES**

www.advmatinterfaces.de

[37] G. W. Mudd, M. R. Molas, X. Chen, V. Zólyomi, K. Nogajewski, Z. R. Kudrynskyi, Z. D. Kovalyuk, G. Yusa, O. Makarovsky, L. Eaves, M. Potemski, V. I. Fal'ko, A. Patanè, *Sci. Rep.* **2016**, *6*, 39619.

[38] L. de Brucker, M. Moret, B. Gil, W. Desrat, *AIP Adv.* **2022**, *12*, 055308.

[39] D. J. Terry, V. Zólyomi, M. Hamer, A. V. Tyurnina, D. G. Hopkinson, A. M. Rakowski, S. J. Magorrian, N. Clark, Y. M. Andreev, O. Kazakova, K. Novoselov, S. J. Haigh, V. I. Fal'ko, R. Gorbachev, *2D Mater.* **2018**, *5*, 041009.

2301086 (12 of 12)